We are IntechOpen,
the world's leading publisher of
Open Access books
Built by scientists, for scientists

6,900
Open access books available

186,000
International authors and editors

200M
Downloads

154
Countries delivered to

Our authors are among the

TOP 1%
most cited scientists

12.2%
Contributors from top 500 universities

BOOK CITATION INDEX
CLARIVATE ANALYTICS
INDEXED

WEB OF SCIENCE™

Selection of our books indexed in the Book Citation Index
in Web of Science™ Core Collection (BKCI)

Interested in publishing with us?
Contact book.department@intechopen.com

Switched Reluctance Motor Modeling and Loss Estimation Review

Pedro Sousa Melo and Rui E. Araújo

Abstract

Switched reluctance machines (SRM) are an alternative to conventional and permanent magnet (PM)-based machines. They are simple, robust and fault tolerant, and able to reach very high speeds with high efficiency. However, they operate with high torque pulsation and are noisy. Also, a nonconventional power converter type and specific control schemes must be included. Furthermore, SRM operation is characterized by high nonlinear features, which makes it difficult to be modeled and controlled. SRM energy conversion principles are a keystone to understand its operation. SRM efficiency increases with speed, where core and mechanical losses are more significant. For this machine, core loss estimation is a complex task, due to the nonlinear behavior of the magnetic materials. In addition, flux waveforms are not sinusoidal and particular waveforms appear in different core sections. Empirical formulas are usually considered in core loss estimation, but this is insufficient for SRM.

Keywords: SRM geometric and magnetic features, modeling, energy balance, torque production, loss characterization

1. Introduction

Switched reluctance machines (SRM) have been recognized as an alternative to conventional AC and DC motor drives. They have a multi-domain potential, such as electric vehicle, household appliances, aircraft industry, and servo system, to name a few examples [1]. They are simple, rugged, and fault-tolerant machines, with low cost. Moreover, they can reach very high speeds with high efficiency, since there are no windings or permanent magnets (PM) in the rotor [2]. A considerable attention to SRM drives has been given by both industry and research community, mainly due to the absence of PM. Limitations on rare-earth element availability and their increasing cost are the main reasons, since those elements are fundamental in PM composition [1]. Nonetheless, there are some drawbacks that need to be tackled: they have high torque pulsation and noisy operation. Also, a nonconventional power converter type with specific control schemes must be included. Furthermore, its efficiency (low speed) and power density are lower than in PM machines [3, 4].

SRM modeling is fundamental for two basic reasons: design and control development. In the first one, reducing prototype costs, while optimizing its design (e.g., better efficiencies with reduced torque ripple and noise), is a crucial goal [5]. On the

other hand, coupling the SRM model with power converter and load models is fundamental for developing better control algorithms [1].

SRM operate under strong nonlinear conditions, where modeling can be a very challenging task. Finite element analysis (FEA) is a very accurate but time-consuming method. Analytical models and lookup tables are much faster but have reduced accuracy. Therefore, SRM modeling must be addressed as a trade-off between simulation accuracy and computational speed [6].

For any electrical machine, loss estimation is fundamental for design optimization and control. Furthermore, an accurate loss evaluation is vital for achieving the desired operation conditions [7]. Like in other electric machines, SRM losses occur in stator windings, core materials (stator and rotor), and mechanical moving parts. In high-speed operation, where SRM has better performances, core losses have a significant weight, together with the mechanical ones. Iron loss estimation in SRM is a complex task, mainly due to nonlinearities of the magnetic core. In addition, flux density waveforms are not sinusoidal, and different ones must be considered in several magnetic circuit parts, depending on the machine geometry [8]. Moreover, those waveforms are conditioned by control features.

This chapter is structured as follows: Section 2 starts with an overview on reluctance machines. Next, fundamental geometric and magnetic features, for conventional SRM, are addressed. Operation principles are discussed, highlighting the correlation between machine features and control parameters. In Section 3, energy conversion is deeply analyzed, based on a lumped parameter model. The focus is given to torque production mechanism. Section 4 addresses SRM losses, where common methods for SRM loss estimation are discussed. The impact of sinusoidal and nonsinusoidal flux density waveforms is also discussed.

2. SRM characterization

This section intends to present a general SRM overview. Several subjects are addressed, starting with the main advantages and drawbacks. Geometric and magnetic features, as well the operation principles, are also discussed.

2.1 Reluctance machines (RM) and SRM basic features

For every RM, torque production is a consequence of rotor movement to a position where the self-inductance of the excited winding is maximized (i.e., minimum magnetic reluctance). The motion may be rotary or linear, and the rotor may be interior or exterior [9]. This is a different principle from conventional machines, such as induction, synchronous (cylindrical rotor), or DC motors, where torque development results from the combination of two magnetic fields (stator and rotor).

Stator and rotor magnetic circuits are made of laminated soft magnetic iron. Generally, windings are located only in stator, consisting in several electrically independent phase circuits. They may be excited separately (e.g., SRM and stepper motor) or together (e.g., synchronous reluctance motor, SRM, and stepper motor). The rotor has no windings or permanent magnets, and its shape has a significant role in maximizing the phase inductance variation with its position. In fact, all these machines have in common a magnetic circuit with deep anisotropic features. The rotor simplicity is the main advantage when compared to permanent magnet or rotor winding machines. The manufacturing cost can be lower than in other types of motors; also, the reliability and robustness are improved and rotor cooling is not so
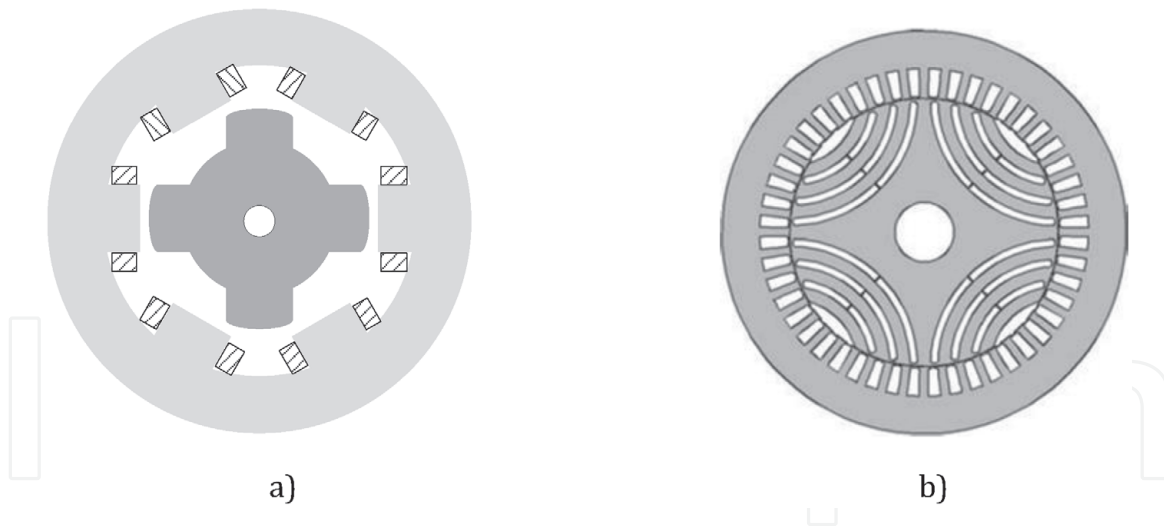
Figure 1.
(a) Three-phase SRM (6/4) and (b) Synch_RM.

critical [9]. **Figure 1** depicts the basic structure of SRM and synchronous reluctance motor (Synch_RM):

- SRM higher simplicity can be observed: stator winding coils are concentrated around its salient poles (N_s); usually, diametrically opposite windings are connected in series. Motor phases can be formed by one of these pairs or groups of pairs. The rotor geometry has also a set of salient poles (N_r)—in this case $N_s = 6$ (two poles/phase), while $N_r = 4$.

- Synch_RM has an AC conventional slotted stator, where the windings are sinusoidally distributed. **Figure 1(b)** represents a four-pole rotor with axially magnetic laminations.

Although SRM presents a similar structure when compared to variable reluctance (VR) stepper motors, there are important differences that should be highlighted: usually SRM have a small pole number, with a larger stepping angle. Most often, the rotor has a continuous movement, and its output power is much higher than in VR stepper motor [9].

In conventional SRM design, stator and rotor poles features are usually attached to the following conditions:

$$N_s > N_r \tag{1}$$

$$\beta_r \geq \beta_s \tag{2}$$

$$\varepsilon = \frac{1}{m} \cdot \frac{2\pi}{N_r} \tag{3}$$

$$\varepsilon < \text{Torque Zone} < \beta_s \tag{4}$$

$$m = \frac{N_s}{N_s - N_r} \tag{5}$$

where N_s and N_r are, respectively, the stator and rotor poles (even numbers); β_s and β_r are, respectively, the stator and rotor pole arcs; ε is the stroke angle, i.e., the rotor displacement due to a single pulse current; and m is the SRM phase number.

The denominator in Eq. (3) gives the total phase pulses/revolution, while Eq. (4) assures the motor can start, independently of rotor initial position. For an m-phase

m	N_s	N_r
3	6	4
3	12	8
4	8	6
5	10	8
6	12	10
7	14	12

Table 1.
SRM phase and poles configurations.

SRM, there are several (N_s; N_r) combinations, according to Eqs. (1) and (5). **Table 1** shows the most common configurations.

Usually, the average torque is higher for large N_s and N_r, with a smaller ripple. However, the number of power devices (switches and diodes) in the converter will increase. Therefore, the cost is higher, as well the switching losses. Conduction time is also higher, which increases copper losses. In addition, since phase current frequency (f_s) is given by $f_s = \omega_r * N_r$ (ω_r: rotor angular speed), core losses will be higher. Nevertheless, torque ripple filtering becomes easier, due to its higher frequency [10].

2.2 SRM background and development

The SRM drives for industrial applications are relatively recent. Although the earliest recorded SRM is from 1838 [9], its actual development stage would not be possible without the semiconductor-based solid-state power switching technology in the early 1960s. This brought a huge interest in new machine development, as well in control methods, where the SRM is included.

In the last 40 years, different configurations of reluctance motor and switching methods have been investigated, both theoretically and experimentally. This is quite clear when the 67 worldwide registered patents on SRM before 1976 are compared to the 1755 ones, between 1976 and 1999 [11]. According to this reference, the total number of papers published in these periods increased from 11 to 1847, respectively. Presently, most significant SRM patents are the basis for its manufacture. The development of digital control and power electronics has made possible to exploit in an effective way the SRM characteristics [11].[1]

From the power conversion perspective, the SRM main disadvantage is related to the absence of permanent magnets and windings in the rotor: the machine power density is limited by the single stator excitation source [10]. Also, due to the magnetic circuit geometry, the machine is very sensitive to the effects of fringing fields and magnetic saturation. This introduces high nonlinear features that must be considered in SRM operation. A power converter and a controller must be integrated with the SRM, since phase currents are electronically commutated. The consequent pulsed magnetic fields have a major contribution in torque ripple and acoustic noise, which are the main drawbacks of SRM drives [12]. In order to tackle these drawbacks, research efforts have been focused on control strategies [13, 14], but machine design [15] and power converter structure [16] have also been addressed.

Another relevant SRM particularity is a small phase mutual inductance. In many applications it is considered null, i.e., each phase is magnetically independent from

---

[1] Chapter 2 of this reference includes an interesting and detailed overview on SRM historic development.

each other. This has a deep impact on the machine operation: since a phase fault has no influence in the other ones, SRM have a significant fault-tolerance capacity. As phase number increases, the smaller is the impact of a faulted phase. However, in high-speed operation, currents in adjacent phases can overlap for a significant portion of the conduction cycle. Therefore, the mutual flux linkages between phase windings can be most relevant, so their effects should be considered. This suggests that different model and control approaches must be addressed, whether SRM is operating in low or high speeds.

2.3 Geometric specifications

SRM phase inductance depends on both the current (due to saturation effect) and rotor position (θ). The unsaturated values of the aligned inductance (L_a) and the unaligned inductance (L_u) are fundamental in SRM basic theory, in particular the ratio L_a/L_u [9]. In addition, the machine geometric features have also a significant role, particularly the size and shape of stator and rotor poles, as well the air gaps. **Figure 2** depicts some of the most relevant geometric parameters, given by:

$$\tau_s = \frac{2\pi}{N_s} \tag{6}$$

$$\tau_r = \frac{2\pi}{N_r} \tag{7}$$

$$\theta_s = 2\pi \left(\frac{1}{N_r} - \frac{1}{N_s} \right), with \ N_s > N_r \tag{8}$$

The stator and rotor pole pitch are, respectively, τ_s and τ_r, where θ_s is the phase shift between successive stator phase inductances. It can easily be seen that $\theta_s = \varepsilon$, by substituting Eq. (5) in Eq. (3).

2.4 Magnetic features

Figure 3 represents a set of magnetization curves, for one phase of an SRM, where each one is related to a different rotor position (θ). The aligned and
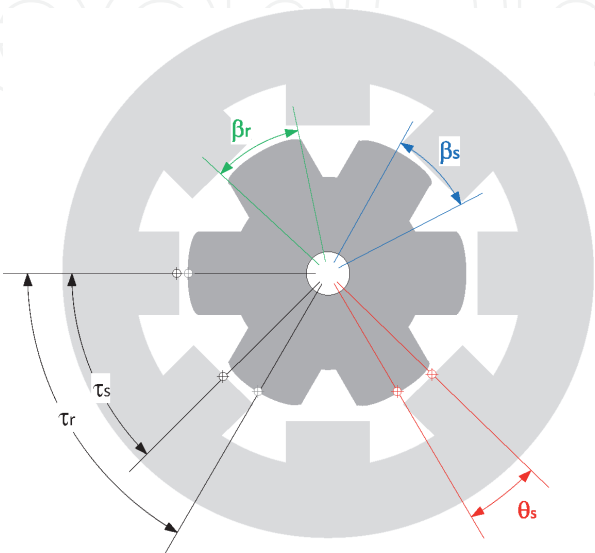

Figure 2.
SRM geometric features.

unaligned positions are the set limits. Also, the influence of magnetic saturation is visible.

Admitting uniform flux density, with no flux leakage and no saturation/hysteresis effect, the phase inductance can be approximated by:

$$L_s = N_s^2 \cdot A(\theta) \left[2 \cdot \left(\frac{l_p}{\mu_{fe}} \cdot \frac{A(\theta)}{A_p} + \frac{l_0}{\mu_0} \right) + \frac{l_y}{\mu_{fe}} \cdot \frac{A(\theta)}{A_y} \right]^{-1} \tag{9}$$

where: μ_{fe} and μ_0 are, respectively, the core material and the air magnetic permeability; A_p is the cross section of one stator and rotor magnetic pole (considering similar sections); A_y is the cross section of one yoke section (considering similar sections); l_p is the phase linkage flux longitudinal length in stator pole + rotor pole path; l_0 is the phase linkage flux longitudinal length in the air gap path; l_y, is the phase linkage flux longitudinal length in yoke path between two stator magnetic poles.

Under the previous conditions, for both the aligned and unaligned position, one has $A(\theta)$ = A_p. The airgap term in Eq. (9) denominator is dominant, so l_0 has a profound impact in L_a and L_u. Moreover, since SRM anisotropic features play a fundamental role on its performance, maximizing L_a/L_u is crucial in SRM design. In order to increase L_a, the correspondent l_0 should be as small as possible. This highlights the fact that SRM aligned air gap must be tighter than for other machines. As a consequence, manufacture imperfection or rotor eccentricity will have a considerable negative impact in SRM operation [7].

From **Figure 3**, it can be seen that $L_s(\theta)$ gradient is more relevant in the overlapping region, meaning that this is the most relevant torque production zone. In the overlapping regions, L_s varies approximately linearly with θ. Thus, it is reasonable to admit $A(\theta)$ as:

$$A(\theta) = l \cdot R \cdot \theta, \, 0 < \theta < \beta_r \tag{10}$$

where $l \approx$ machine's axial length; R $\approx$ rotor pole radius; β_r rotor pole arc.

Nonetheless, it should be noted that A(θ) is in fact much dependent on the machine pole shape.
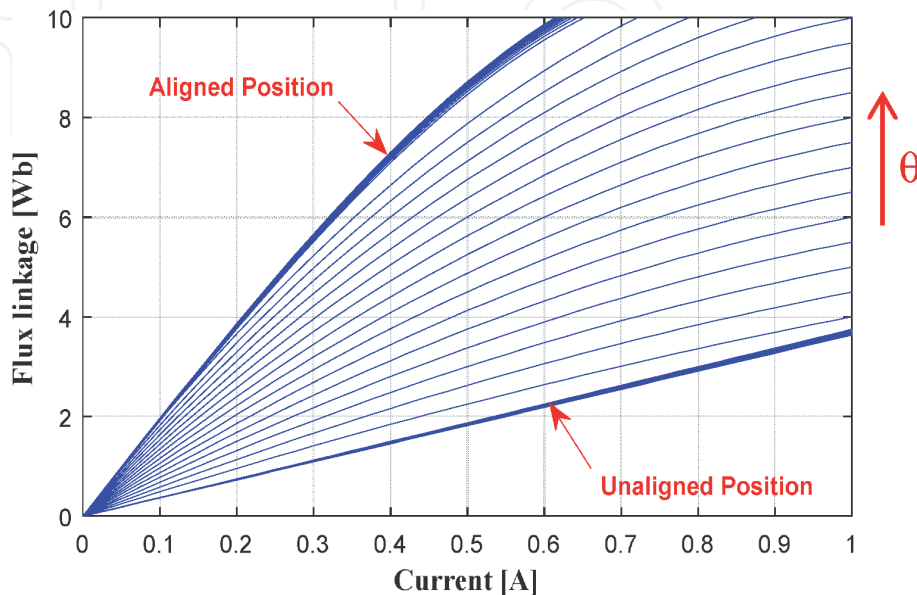

Figure 3.
SRM magnetic characteristics (single-phase) for different θ.

2.5 SRM operation fundamentals

Torque production conditions can be seen in **Figure 4**, where an elementary single-phase machine is depicted, for different rotor positions.

In (a), rotor poles are perfectly aligned with the stator phase poles, where its inductance is maximum. Thus, no torque is produced. The rotor unaligned position is depicted in (d): its interpolar axis is aligned with the stator poles. The torque has a null value, since the rotor poles are displaced in an equivalent position related to the stator poles (here the phase inductance is minimum, since magnetic reluctance is maximum). As the rotor moves from the unaligned position and comes closer to any stator pole, the torque is no longer zero and tries to align the rotor with that particular stator pole: in (b) and (c), the developed torque tends to bring the rotor back to (a) position—this is a stable equilibrium position, while (d) is an unstable equilibrium position [9]. Torque direction is contrary in (b) and (c), which highlights the fact that switching currents in stator windings must be implemented according to the rotor position—it becomes clear that stator phases must be energized for rotor position between maximum and minimum phase inductance. This elementary machine highlights three important SRM general features [9, 10]:

    i. In order to avoid situations (a) and (d) in **Figure 4**, all SRM verify the condition: $N_s \neq N_r$. In those positions the motor is not able to start when stator phase is excited.
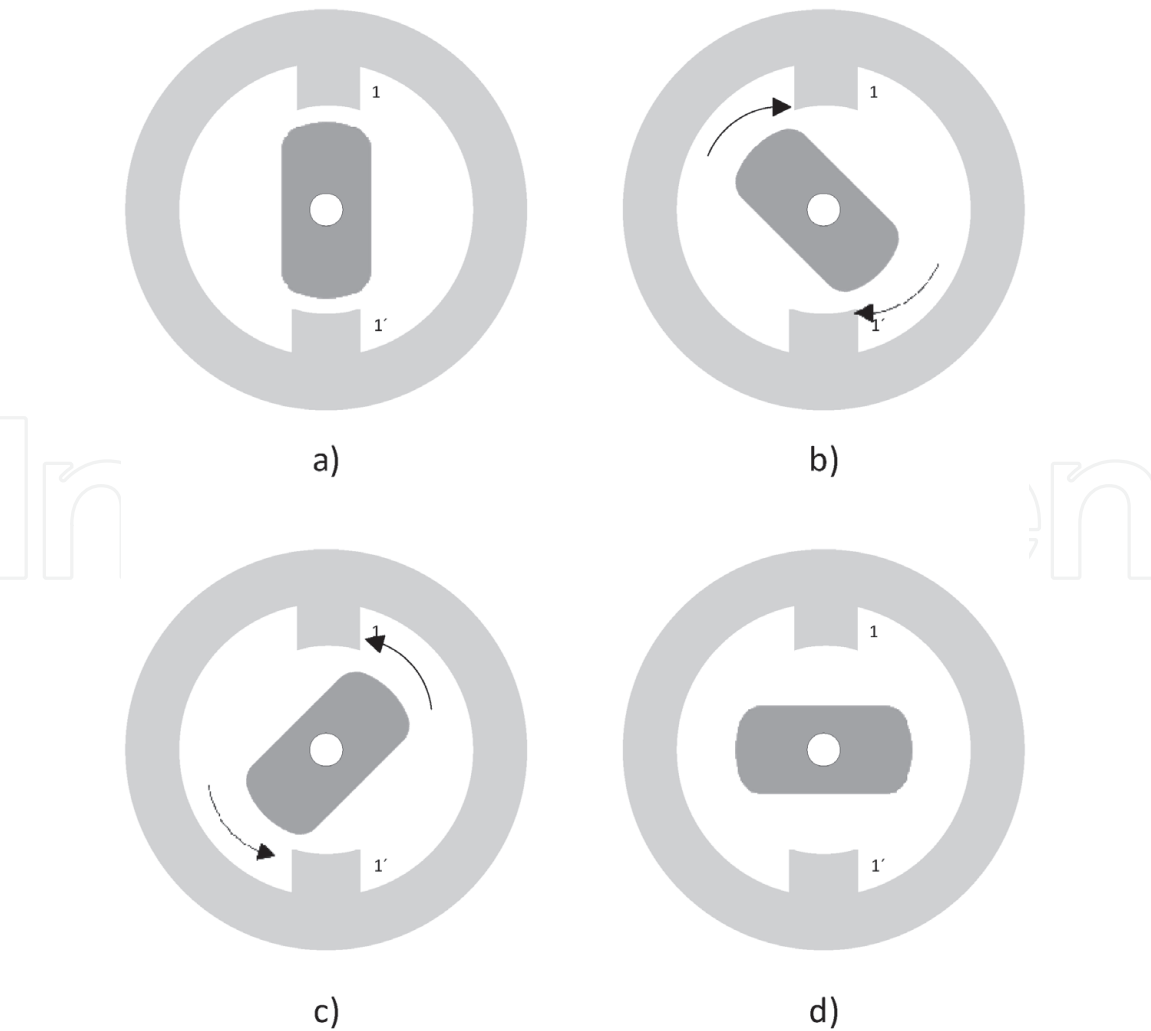

Figure 4.
Rotor positions of an elementary SRM.

ii. Torque is produced by sequentially switching the currents in the stator phase windings when there is a variation of reluctance, which depends on rotor position. This is the reason why a controlled power converter supply system is mandatory with rotor position feedback. Therefore, SRM operation is always implemented with a converter + controller (SRM drive).

iii. Winding current polarity has no influence in torque development, since this is a reluctance torque.

The fundamental concepts in correlating SRM rotor position to its control are depicted in **Figure 5**. Phase current ($I(\theta)$) is represented for both motor and generator SRM modes, as well the torque production zones ($T(\theta)$). Except for the red $L_s(\theta)$ curves which denote saturation effect, all the others assume ideal conditions (no saturation and hysteresis; ohmic winding resistance is zero).

It can be seen that L_s is a periodic function of θ, with period τ_r.[2] The following expressions can be considered:
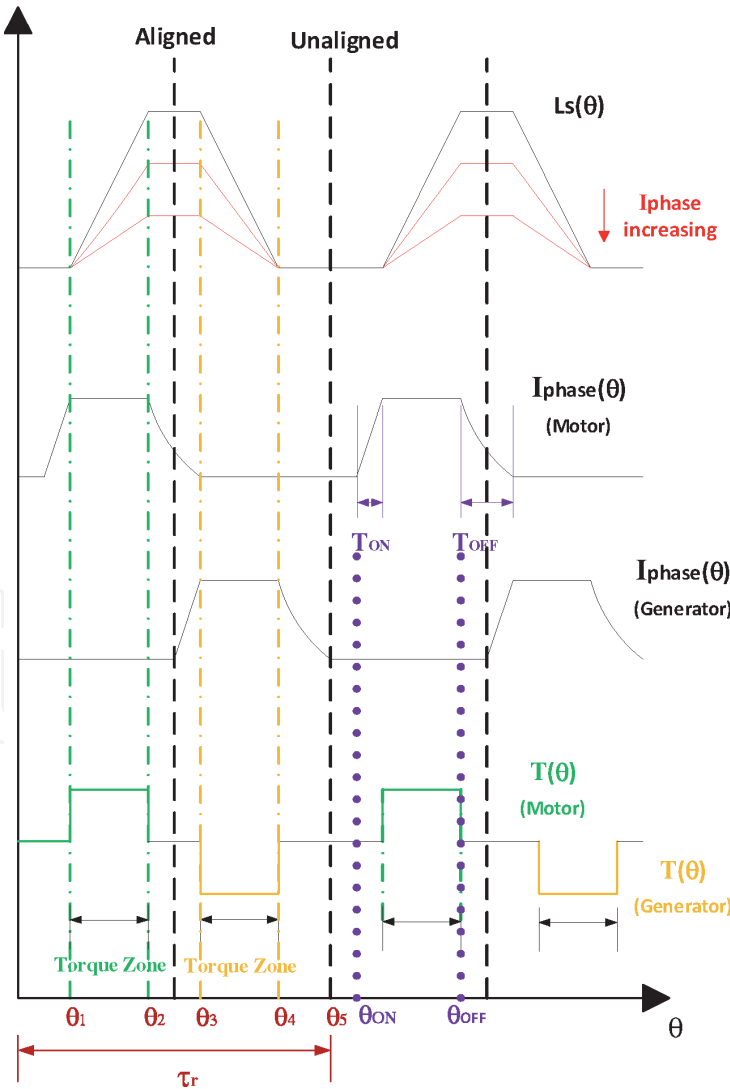

Figure 5.
L_s profile, current pulses (motor and generator), and torque zones.

_____

[2] $L_s(\theta)$ origin is at the unaligned rotor position.

$$\theta_1 = \frac{\pi}{N_r} - \left(\frac{\beta_s + \beta_r}{2}\right) \qquad (11)$$

$$\theta_2 - \theta_1 = \beta_s \qquad (12)$$

$$\theta_3 - \theta_2 = \beta_r - \beta_s \qquad (13)$$

$$\theta_4 - \theta_3 = \beta_s \qquad (14)$$

$$\theta_5 - \theta_4 = \frac{\pi}{N_r} - \left(\frac{\beta_s + \beta_r}{2}\right) \qquad (15)$$

The instantaneous torque is controlled by current amplitude regulation and the switching instants (θ_{ON} and θ_{OFF}). In addition, rotor speed has also a significant impact on control modes.

The $L_s(\theta)$ top flat zone is related to the difference between the stator and rotor pole arcs, respectively, β_s and β_r: as it tends to zero, the top flat becomes narrower. Although this is a "dead zone" since there is no energy conversion (torque is null), it might help to avoid braking torque in the demagnetizing period (T_{OFF}). It should be emphasized the unidirectional current polarity in both modes. Torque development is clearly associated to $dL_s/d\theta \neq 0$ (i.e., the overlapping poles regions); it is associated to motor (+) and generator (−) modes. This stresses the fact that current impulse rise (T_{ON}) and fall (T_{OFF}) periods have a fundamental role in SRM operation features: T_{ON} must be as small as possible, while current should reach its maximum when stator and rotor poles start to overlap. As for T_{OFF} (the defluxing period), it depends on how fast the energy stored in the linkage magnetic field can be turned to zero. Therefore, T_{OFF} limits must assure a zero current at the beginning of the $dL_s/d\theta < 0$, in order to avoid a braking torque. These are important issues that must be addressed by the drive controller.

The SRM core magnetic features, together with pole geometry, have a fundamental role in the $L_s(\theta)$ profile. This is crucial in estimating θ_{ON} and θ_{OFF} values. Moreover, magnetic characteristics are particularly influenced by local saturation in stator and rotor poles, which also depends on SRM operation conditions.

Phase current commutation, in addition to SRM geometry, is responsible for torque ripple components. This contributes for increasing the complexity demanded to the SRM drive controller.

In short, the phase current pulse waveform as a function of θ, in addition to θ_{ON} and θ_{OFF}, plays a keystone role in all SRM operation modes. Therefore, the machine must be integrated with the power converter and the controller, working as a single system.

3. SRM modeling and energy balance

SRM can be modeled in a similar way as for conventional electrical machines. Therefore, a model based on lumped parameters can be a first option. However, depending on the purpose (e.g., design or control), particular attention should be addressed when applying conventional methods for modeling this machine, due to its specific nonlinear operation features.

Nonetheless, this section intends to address the SRM energy conversion principles, where a lumped parameter approach is well suited. The mathematical model is based on the following equations:

- Voltage equation

$$V_{phase} = R_s \cdot i + \frac{d\Psi(i,\theta)}{dt} \tag{16}$$

where R_s, i, and $\Psi(i,\theta)$ are, respectively, the stator phase resistance and current and flux linkage.[3]

- Magnetic equation

$$\Psi(i,\theta) = L_s(i,\theta) \cdot i \tag{17}$$

where $L_s(i,\theta)$ is the stator phase self-inductance.

- Electromechanical equation (instantaneous torque)

$$T_e = \sum_{j=1}^{m} T_j(i,\theta) \tag{18}$$

where T_j is the torque developed by phase j and m is the SRM phase number.

- Mechanical equation

$$T_e - T_{load} = J\frac{d\omega r}{dt} + K_f \omega r \tag{19}$$

where T_{load} is the mechanical load, J is the system inertia, ωr is the instantaneous rotor mechanical angular speed, and K_f is the viscous friction coefficient, due to bearing lubricant fluid.

It should be noted that magnetic feature complexity is not entirely depicted in **Figure 3** (flux density waveforms in different SRM sections cannot be addressed). The high complexity of SRM modeling lies in Eq. (17), which has a significant impact on torque production, since it depends on the magnetic anisotropic features. In order to take a deeper insight on Eq. (18), the torque production mechanism is now analyzed with more detail.

3.1 Electromechanical energy conversion and torque production

Since SRM are electromechanical energy converters, a review on energy balance relationships is first addressed. An electromechanical system is based on an electrical system, a mechanical system, and a coupling field (i.e., electromagnetic and electrostatic fields), common to both systems. From this interaction, energy can be transferred from one system to the other. It should be noted that both coupling fields can exist simultaneously, while the electromechanical system may have several electrical and mechanical subsystems. Different losses by heat dissipation occur in the electrical and mechanical systems, as well in the coupling field. Several phenomena contribute to this [17]:

- Electrical losses, due to current-carrying conductor ohmic resistance

- Mechanical losses, due to friction of moving parts

---

[3] Phase mutual influences and leakage flux are neglected.

- Magnetic losses in the core ferromagnetic materials (magnetic fields) and dielectric losses (electric fields)

Figure 6 depicts the energy balance in an elementary electromechanical system—according to the energy conservation principle (first thermodynamic law)—where losses and stored energy components are represented.

The black dotted arrows represent the adopted convention for positive W's. The energy balances for the electric and mechanical systems are then expressed as:

$$W_E = W_{eL} + W_{eS} + W_{ef} \tag{20}$$

$$W_M = W_{mL} + W_{mS} + W_{mf} \tag{21}$$

where *WE* is the energy supplied by the electrical source, *WeL* is the electrical losses, *WeS* is the energy stored in the fields (electric or magnetic) not coupled with the mechanical system, and *Wef* is the energy transferred to the coupling field from the electrical system. In a similar way, *WM* is the energy supplied by the mechanical source, *WmL* is the mechanical losses, *WmS* is the energy stored in the moving parts of the mechanical system, and *Wmf* is the energy transferred to the coupling field from the mechanical system. The colored arrows represent the physical energy flux: except for the losses (irreversible phenomena), all the W's flux can be reversible, depending on the system operation. From **Figure 6** it can be seen that:

$$W_{ef} + W_{mf} = W_f + W_{fL} \tag{22}$$

where *Wf* is the energy stored in the coupling field and *WfL* is the loss energy within the coupling field. Combining Eq. (20) and Eq. (21) gives:

$$W_E + W_M = (W_{eL} + W_{mL}) + (W_{eS} + W_{mS}) + (W_{ef} + W_{mf}) \tag{23}$$

From this point, only electromagnetic coupling field are considered. Rearranging Eq. (23) gives:

$$W_E = (W_{eL} + W_{eS}) + (W_{ef} + W_{mf}) + (-W_M + W_{mL} + W_{mS}) \tag{24}$$

The magnetic coupling field will be addressed as a conservative field, in order to take advantage of a fundamental property: the energy stored in a conservative field depends only on state variable values, and not on the transition between states. The sum of potential and kinetic energy is constant; therefore, the losses are null (i.e., $W_{fL} = 0$). It should be noted that, for the purpose of this analysis, such approach is quite acceptable, since the most significant part of the stored energy in the coupling
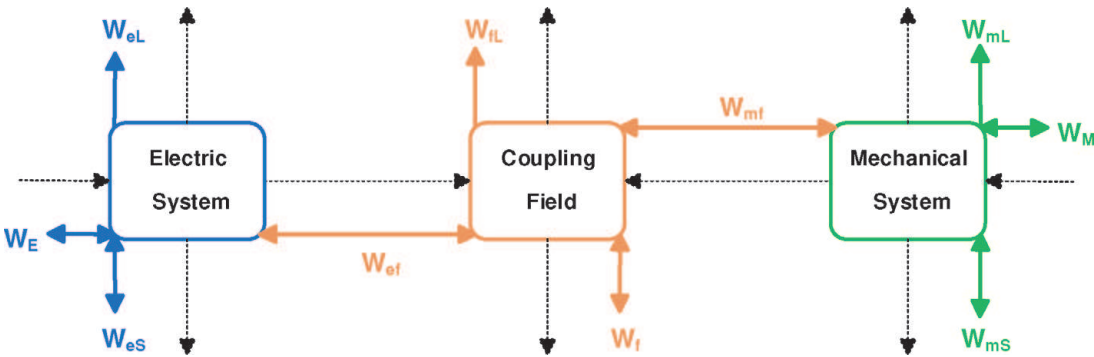

Figure 6.
Energy flux (colored arrows) in an electromechanical system.

fields is in the air gaps of the electromechanical device. Air is a conservative medium; thus the energy stored there can be returned to the electrical or mechanical systems. Finally, Eq. (24) can be written as:

$$W_E = W_{eL} + W_{eS} + W_f - W_{mf} \tag{25}$$

where:

$$W_f = W_{ef} + W_{mf} \tag{26}$$

$$-W_{mf} = -W_M + W_{mL} + W_{mS} \tag{27}$$

The voltage equation for a generic electric system (one phase) is given by Eq. (16). For convenience of analysis, it is written again as:

$$v = r \cdot i + \frac{d\Psi(i, \theta)}{dt} \tag{28}$$

Therefore, Eq. (25) can be expressed as:

$$\int v \cdot i \cdot dt = \int r \cdot i^2 \cdot dt + \int \frac{d\Psi(i, \theta)}{dt} \cdot i \cdot dt \tag{29}$$

Since $\Psi(i, \theta)$ is the flux linkage, the effect of leakage inductance is neglected. Therefore, $W_{eS} = 0$ and the following differential equation can be extracted:

$$dW_E = dW_{eL} + dW_f - dW_{mf} \tag{30}$$

$$dW_E = v \cdot i \cdot dt \tag{31}$$

$$dW_{eL} = r \cdot i^2 \cdot dt \tag{32}$$

$$dW_f - dW_{mf} = d\Psi(i, \theta) \cdot i \tag{33}$$

$$dW_{mf} = -T \cdot d\theta \tag{34}$$

It is important to stress that $\Psi(i, \theta)$ is a single-value function, since it represents a conservative field. Therefore, hysteresis is not included here, but saturation can be considered—this is the reason for having "*i*" as an independent variable. With θ as the other independent variable, one has:

$$d\Psi(i, \theta) = \frac{\partial \Psi(i, \theta)}{\partial i} di + \frac{\partial \Psi(i, \theta)}{\partial \theta} d\theta \tag{35}$$

Substituting this in Eq. (33) yields:

$$\underbrace{dW_{ef} + dW_{mf}}_{dW_f} - dW_{mf} = \frac{\partial \Psi(i, \theta)}{\partial i} i di + \frac{\partial \Psi(i, \theta)}{\partial \theta} i d\theta =$$

$$= \underbrace{\frac{\partial \Psi(i, \theta)}{\partial i} i di + [1 - \alpha(i, \theta)] \cdot \frac{\partial \Psi(i, \theta)}{\partial \theta} i d\theta \cdot i}_{dW_f} + \underbrace{\alpha(i, \theta) \cdot \frac{\partial \Psi(i, \theta)}{\partial \theta} i d\theta}_{-dW_{mf}}$$

$$\tag{36}$$

The function $\alpha(i, \theta)$ allows a general formulation for infinitesimal variations in the coupling field stored energy and the mechanical energy. However, analytical expressions for $\alpha(i, \theta)$ are difficult to get. At this point, it is convenient to define the coenergy function (W_c) as:

$$W_c(i, \theta) = \int \Psi(i, \theta) \cdot di \tag{37}$$

Under this condition, $W_f(i, \theta)$ is given by:

$$W_f(i, \theta) = \int i \cdot d\Psi \tag{38}$$

Both $W_c(i, \theta)$ and $W_f(i, \theta)$ are represented in **Figure 7** ($i: 0 \rightarrow i_1$, $\theta = constant$). From **Figure 7**, it can be seen that (for $i = constant$).

$$\Psi(i, \theta) \cdot i = W_f(i, \theta) + W_c(i, \theta) \tag{39}$$

Taking Eq. (39) θ derivative, one has:

$$\frac{\partial \Psi(i, \theta)}{\partial \theta} i = \frac{dW_f(i, \theta)}{d\theta} + \frac{dW_c(i, \theta)}{d\theta} \tag{40}$$

In order to take an insight over the torque production in an SRM, the analysis is now addressed taking $di = 0$. Under this condition, Eq. (36) is written as:

$$\frac{\partial \Psi(i, \theta)}{\partial \theta} i d\theta = dW_f - dW_{mf} \tag{41}$$

$$\frac{\partial \Psi(i, \theta)}{\partial \theta} i = \frac{dW_f(i, \theta)}{d\theta} - \frac{dW_{mf}(i, \theta)}{d\theta} \tag{42}$$

Finally, from Eq. (40), Eq. (41), and Eq. (34), the torque developed by a single phase (T) is given by:

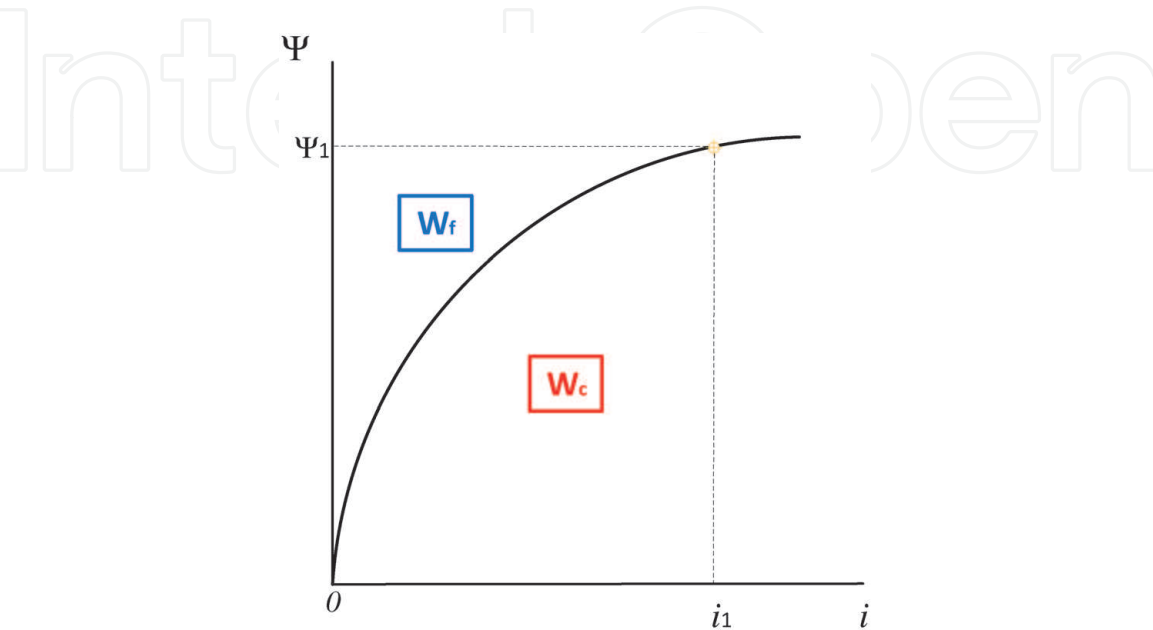$$T = \frac{dW_c(i, \theta)}{d\theta}, for \ i = constant \tag{43}$$

Figure 7.
Stored energy and coenergy in a magnetic field.

13

For a generic SRM with m phases, the total electromagnetic torque is:

$$T_e = \sum_{j=1}^{m} \frac{\partial W_c^j(i,\theta)}{\partial \theta}, \quad i = constant \tag{44}$$

where W_c^j is the coenergy related to the stored magnetic field of phase j and m is the SRM phase number. This highlights the fact that torque production is in close relation with the core magnetic properties, for each rotor position (θ). The average torque (T_{av}) can be calculated by integrating T_e:

$$T_{av} = \frac{1}{\varepsilon} \int_0^\varepsilon T_e \cdot d\theta \tag{45}$$

A geometric representation may help to clarify how energy is transferred between the electrical domain, the magnetic coupling field, and the mechanical domain. **Figure 8** includes two magnetic characteristics for two rotor positions, θ_a and θ_b.
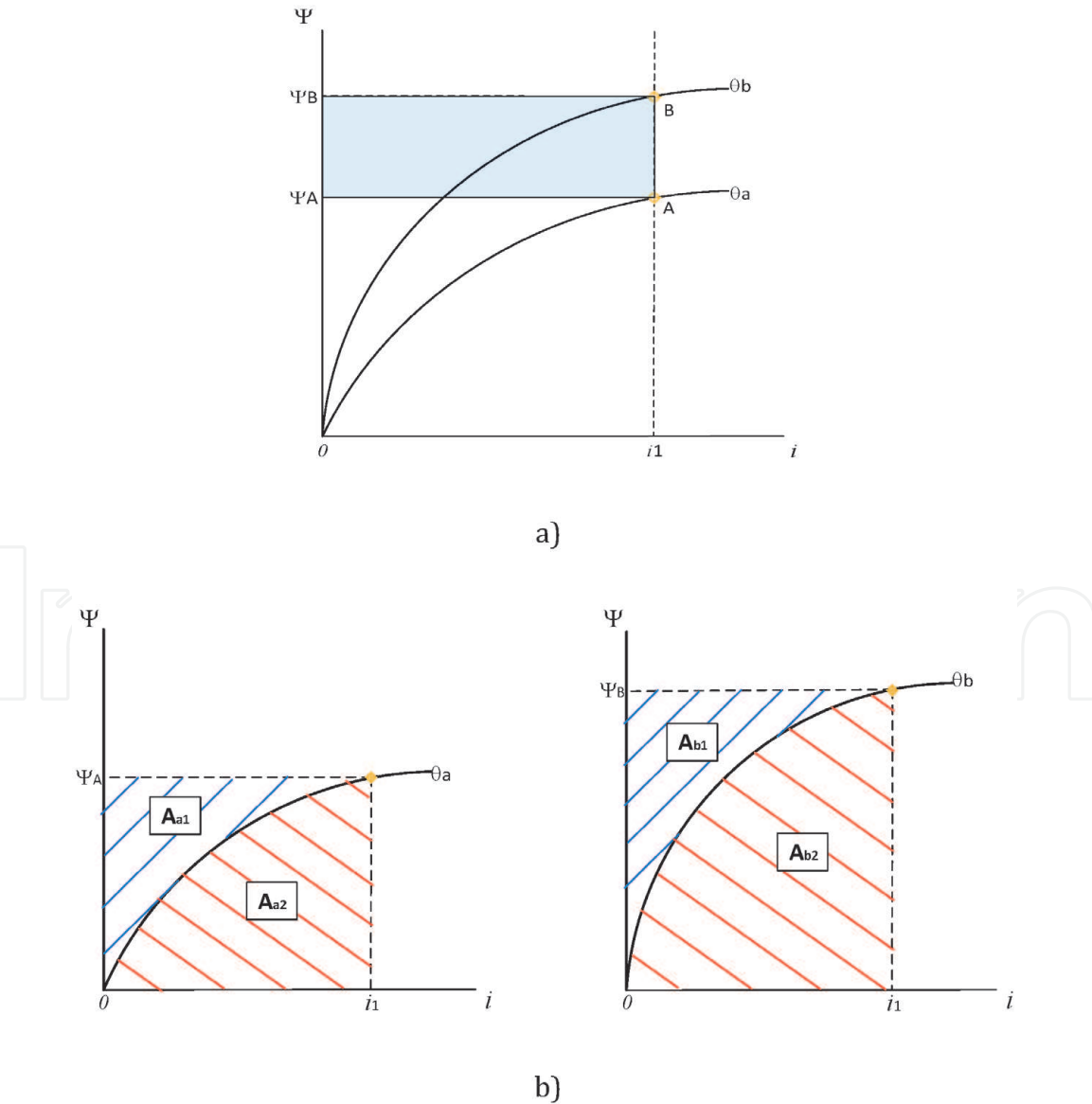

a)

b)

Figure 8.
(a) Magnetic characteristics for θ_a and θ_b (i = constant). (b) Stored magnetic and coenergy distribution for θ_a and θ_b (i = constant).

For $i = i_1$, $\Delta W_{source}(i_1, \theta) = i_1 \cdot (\Psi_B - \Psi_A)$ is the energy transferred to the magnetic coupling field from the electrical source, for a rotor position displacement from θ_a to θ_b (A $\rightarrow$ B in **Figure 8(a)**. This is related to the difference between rectangles [0-i_1-B-Ψ_B] and [0-i_1-A-Ψ_A] (i.e., the blue rectangle). From **Figure 8(b)**, it can be seen that this difference is given by:

$$\underbrace{(A_{b1} - A_{a1})}_{\Delta W_{stored\_coupling\_field}(i_1, \theta_A \rightarrow \theta_B)} + \underbrace{(A_{b2} - A_{a2})}_{\Delta W_c(i_1, \theta_A \rightarrow \theta_B)} \tag{46}$$

(A_{a2} and A_{b2} are the coenergy (W_c) related to, respectively, θ_a and θ_b.)
Therefore:

$$\Delta W_{source}(i_1, \theta_A \rightarrow \theta_B) = \Delta W_{stored\_coupling\_field}(i_1, \theta_A \rightarrow \theta_B) + \Delta W_c(i_1, \theta_A \rightarrow \theta_B) \tag{47}$$

For an infinitesimal energy change ($\theta_A \rightarrow \theta_A + d\theta$):

$$dW_{source}(i_1, \theta) = dW_{stored\_coupling\_field}(i_1, \theta) + dW_c(i_1, \theta) \tag{48}$$

which is similar to Eq. (41).

3.2 Linear magnetic circuit

If no magnetic saturation exists, the magnetization curves are straight lines (for a fixed θ), as represented in **Figure 9**.
Since $\Psi(i, \theta) = L_s(\theta) \cdot i$, from Eq. (35), one has:

$$d\Psi(i, \theta) = L_s(\theta) \cdot di + i \cdot \frac{dL_s(\theta)}{d\theta} \cdot d\theta \tag{49}$$

Therefore, from Eqs. (30) and (33), one has:

$$dW_{source}(i, \theta) = i \cdot L_s(\theta) \cdot di + i^2 \cdot \frac{dL_s(\theta)}{d\theta} \cdot d\theta \tag{50}$$
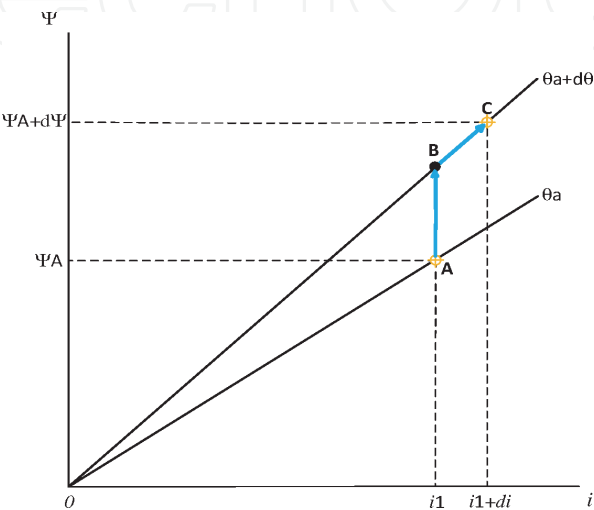
where $dW_{source}(i, \theta) = dW_E - dW_{el}$.

Figure 9.
Magnetic characteristics for θ_a and $\theta_a + d\theta$.

The first and second terms of the second member in Eq. (50) are attached to, respectively, the line segments BC and AB. From Eq. (36), one has:

$$dW_{source}(\text{i}, \theta) = i \cdot L_s(\theta) \cdot di + (1 - \alpha(\text{i}, \theta)) \cdot i^2 \cdot dL_s(\theta) + \alpha(\text{i}, \theta) \cdot i^2 \cdot dL_s(\theta) \quad (51)$$

From **Figure 9**, it can be seen that:

$$\alpha(\text{i}, \theta) = \frac{1}{2} \quad (52)$$

In other words, for *i =constant*, the energy transferred to the magnetic coupling field from the electrical source, as a result of a rotor displacement, is evenly distributed by the stored energy variation in the coupling field and by the coenergy variation (i.e., mechanical energy variation). Finally, Eq. (51) is written as:

$$dW_{source}(i, \theta) = \underbrace{i \cdot L_s(\theta) \cdot di + \frac{1}{2}i^2 \cdot dL_s(\theta)}_{dW_{stored\_coupling\_field}(i, \theta)} + \underbrace{\frac{1}{2}i^2 \cdot dL_s(\theta)}_{dW_c(i, \theta)=dW_{mechanical}(i, \theta)} \quad (53)$$

$$(53)$$

From Eq. (34), the instantaneous torque for a rotor position θ is given by:

$$\text{T} = \frac{1}{2}\frac{dL_s(\theta)}{d\theta} \cdot i^2 \ (i = constant) \quad (54)$$

Some Section 2.5 observations are now more clear from this linear mathematic torque formulation:

- Phase current polarity has no influence in torque production. This is an important feature, since phase current pulses (and flux linkage) can be unipolar. In addition to a simpler controller (compared to other machines drives), iron losses are also smaller.

- Torque development is associated to the growth (+) or decline (−) of stator phase inductance curve ($L_s(\theta)$), respectively, for motor and generator modes.

4. SRM loss characterization

As for any electric machine, SRM models must include losses, since its performance is quite dependable on it. Moreover, all losses should be accurately estimated for different operation modes [18]. Compared to conventional AC machines, this is the most demanding task, particularly for the core losses, because flux density waveforms are not sinusoidal [19]. Similar to other machines, losses in an SRM are related to copper, iron core, and mechanical ones. The machine geometry and operation conditions make SRM loss characterization a nontrivial task.

4.1 Overview on developed SRM loss estimation

Different methods for core loss evaluation in SRM have been investigated by several authors. Using finite elements methods, flux density waveforms are obtained by simulation in [8]. The iron losses were then calculated based on the modified Steinmetz equation. In [18] an analytical method for calculating SRM core losses is proposed. The machine magnetization curves are extracted through finite

element simulation, considering different control strategies. The flux density waveforms in the different parts of the SRM are derived from the flux density waveform of the stator pole, obtained by simulation. The specific core losses are separated into hysteresis, classical eddy current, and excess losses. Their calculation is based on the waveforms and time derivatives of the flux density in each zone. In [20], SRM efficiency is evaluated for continuous operation mode (i.e., current does not extinguish during each phase excitation), but only core losses are considered with more detail (copper losses are calculated through the current *rms* value and the DC phase resistance). Fourier flux density decomposition in the machine core sections is then applied, where core losses are calculated with the modified Steinmetz equation. In order to consider the minor loop influence, a correction factor is included. In [21] a SRM efficiency map is derived based on Fourier flux density decomposition. However, only copper and hysteresis losses are considered. In [22] core losses were calculated through simulation, based on analytic magnetic circuits, considering six different core materials. This approach was validated by comparing the simulation results to experimental ones. However, the paper does not provide information about the magnetic circuit approach.

In the following, an overview on iron loss estimation is addressed, from an engineering perspective. The evolution of the most relevant methods, as well as their merits and limitations, is discussed. Except for [22], the approaches mentioned in the previous paragraph are included here. In the last decades, considerable efforts have been addressing these issues. Nonetheless, further improvements are needed for a precise determination of the flux waveforms and correct calculation of iron loss at nonsinusoidal excitation and nonuniform flux distribution, for a wide range of operation scenarios. This is still an open research field.

As already stated, the focus will be given to iron loss. However, copper losses are usually more significant. Therefore, they are first addressed.

4.2 Copper losses

In the presence of nonuniform electric field (E) and current density (J) distributions, the power dissipated in an arbitrary volume (V) of a conductor is given by:

$$P = \iiint\limits_V \boldsymbol{E} \cdot \boldsymbol{J} \, dV \tag{55}$$

The vector (Ohm's law) is expressed as[4] (vectors $\boldsymbol{E}$, $\boldsymbol{J}$):

$$\boldsymbol{E} = \rho \cdot \boldsymbol{J} \tag{56}$$

Thus, P may be formulated as follows:

$$P = \iiint\limits_V \rho \cdot J^2 \, dV \tag{57}$$

where ρ is the conductor material resistivity ($\Omega \cdot$m). For uniform E and J distributions, Eq. (57) can be written as:

$$P = P_{DC} = R_{DC} \cdot I^2 \tag{58}$$

$I = J \cdot A$ and $R_{DC} = \rho \cdot l / A$ (R_{DC} is the ohmic resistance of the conductor volume (V), where l is the length of the current (I) path inside V and A is the cross-sectional area.

---

[4] Valid for homogeneous and isotropic materials.

An electrical machine winding is made of several coils, where different phenomena may have an impact on winding losses: ρ increases with temperature (*temp*), while the skin (k_{skin}) and proximity (k_{prox}) effects have a relevant impact on J distributions, particularly in high frequencies. All these effects should be included for an accurate winding loss characterization, meaning that Eq. (57) must be considered. For a lumped parameter model approach, as in Section 3, the previous effects are addressed by:

$$P_{AC} = R_{AC} \cdot I^2 \tag{59}$$

where $R_{AC} = R_{DC}$ (*temp*, k_{skin}, k_{prox}).

Therefore, SRM total copper losses can be calculated based on Eq. (59), as the sum of all phase winding losses. Since phase current waveforms are periodic and not sinusoidal (with high frequency), Fourier series may be applied in order to get its harmonic components [23]. It follows that the total winding losses are calculated as:

$$P_w = m \sum_i R_{AC\_i} I_{i\_rms}^2 \tag{60}$$

where m is the phase number and R_{AC_i} and I_{i_rms} are, respectively, the phase AC resistance for the i-order harmonic and the current rms of the i-order harmonic.

In short, copper loss estimation is a relatively simple task, using the stator current. However, the skin and proximity effects require special attention, particularly for high-frequency components. Furthermore, for similar reasons discussed in the next section, Fourier analysis should be carefully applied. Particularly for high loads, temperature influence must also be included.

4.3 Core losses

Usually, lamination manufacturers provide core loss data under sinusoidal excitations in a limited frequency and flux density range. However, this kind of data is not adequate for predicting losses in electrical machines with nonsinusoidal flux waveforms. This requires loss information at high frequencies and high flux densities, particularly for high-speed operation, as in SRM [24].

The development of nonsinusoidal flux density machines and conventional machines fed by power converters (e.g., SR, brushless DC machines, and induction motors with PWM voltages) has motivated researcher's efforts to reach a deeper characterization of magnetic losses under such excitation waveforms. This can be done either by measurement or estimation [19, 24]. New challenges arise for both approaches, since sinusoidal-conventional methods are clearly insufficient. Moreover, since different flux density waveforms are related to particular electric machine configurations, this suggests that specific approaches for characterizing core losses must be addressed, according to the machine type [24].

SRM core loss modeling is a challenging task, since the nonsinusoidal flux density waveforms depend on motor design (geometry and number of stator and rotor poles, yoke geometry, number of phases), operating conditions (conduction angle and mechanical speed influence the magnetic saturation and lamination skin effect level), and the type of control used [18]. Core losses are more significant as speed increases, so for applications like hybrid and electric vehicles, they must be carefully addressed.

Different approaches have been proposed for calculating SRM core losses, from theoretical supported empirical models[5] to physical mathematical models [25]. The later are more accurate, since they take an insight on the core loss physics, aiming to

---

[5] In literature, they are referred as phenomenological models.

describe its nonlinear mechanism under distorted flux [20]. However, they are complex and computationally heavy. From an engineering perspective, empirical models are the preferred ones, due to its simplicity and faster processing. Parameter estimation is based on curve-fitting methods, validated by manufacturer iron sheet data and experimental results or through finite element modeling [20, 24]. Accuracy is much sensitive to parameter values, so their estimation must be attached to specific conditions (e.g., flux density and frequency ranges). Moreover, the manufacturing process of the machine has also a deep impact on core losses; this is very difficult to address in the parameter estimation process [25, 26]. Cutting and punching operations have a relevant influence in the material properties, since they can create inhomogeneous stresses inside the sheets. This depends on the alloy composite, whereas the grain size in the sheets seems to be the main influencing factor [25].

4.3.1 Core loss estimation

Electrical machine core losses can be addressed by three different approaches, in time or frequency domain: empirical equations, loss separation components, and hysteresis models. Only the first two are discussed here.

4.3.1.1 Empirical models based on Steinmetz equation

The Steinmetz coefficients depend on both frequency and flux density [27], so in a waveform with relevant harmonics, it might be difficult to find their values. Based on results of many tests, the classical Steinmetz equation was the first attempt to calculate core loss [28]:

$$P_{core} = C_m f^\alpha B_{max}^\beta \tag{61}$$

where B_{max} is the peak value of the flux density at the lamination, $f = 1/T$ is the remagnetization frequency (T is the hysteretic cycle time interval), and coefficients Cm, α, and β are estimated by fitting the loss model to the lamination manufacturer or measured data. It must be pointed that Eq. (61) assumes sinusoidal flux densities, with uniform distribution across the lamination thickness. Over the years, several upgrades were performed, in order to account for nonsinusoidal waveforms.

The modified Steinmetz equation (MSE) aims to calculate core loss under arbitrary B waveforms. The macroscopic remagnetization rate dM/dt (which is proportional to dB/dt) is directly related to the core losses, as a consequence of wall domain motion [29]. Eq. (61) is then replaced by:

$$P_{core} = \left(C_m f_{eq}^{\alpha-1} B_{max}^\beta \right) f \tag{62}$$

with

$$f_{eq} = \frac{2}{\Delta B^2 \pi^2} \int_0^T \left(\frac{dB}{dt} \right)^2 dt \tag{63}$$

where $\Delta B = B_{max} - B_{min}$.

The MSE has the advantage to highlight the physical origin of the losses, with the same parameters as in Eq. (61). A disadvantage is that it underestimates losses for waveforms with a small fundamental frequency part. Another difficulty is the treatment of waveforms with multiple peaks, in which peak-to-peak amplitude is

not an enough description [29]. In fact, this reflects the increasing MSE limitations, as the flux density moves away from the pure sinusoidal waveform.

The generalized Steinmetz equation (GSE) was also developed from the original Steinmetz equation [29], where losses are calculated in time domain. Here, the instantaneous iron loss is assumed to be a single-valued function of the rate dB/dt and B(t). The inclusion of B(t) allows to consider the DC bias influence in the loss calculation, without additional measurements or curve-fitting functions:

$$P_{core} = \frac{1}{T} \int_0^T C_m \left| \frac{dB}{dt} \right|^\alpha |B(t)|^{\beta - \alpha} dt \qquad (64)$$

For different frequency ranges, different parameter values are necessary. Thus, in the presence of relevant harmonics, the accuracy decays. This is an important drawback, particularly in the presence of minor loops. To overcome this limitation, in [30] the flux density waveform is split into a major loop and minor loop(s), in order to consider the later one effect over loss calculation. Nonetheless, DC bias influence is no longer included. This approach was named improved GSE (iGSE). In [31] a test for loss calculation in nanocrystalline materials, with nonsinusoidal excitation voltage, is reported. Harmonic decomposition was considered, including the phase displacements. According to this reference, iGSE gives better results than GSE.

Both MSE and GSE are applied in time domain. It must be pointed out that the time evolution (history) of the flux density waveform is neglected. This has an impact on the physical phenomena insight, where loss evaluation may be affected.

4.3.1.2 Loss separation method

For a general scenario, the hysteresis loss density related to one cycle, in a particular core part, can be calculated by the following expression:

$$P_h = \frac{f}{m_v} \oint_{B_{min}}^{B_{max}} H dB \qquad (65)$$

where B and H are, respectively, the magnetic flux density and the magnetic flux strength, f is the cycle frequency, and m_v is the density of the ferromagnetic material[6]. The eddy current loss density is derived from Maxwell equations, which is given by:

$$P_e = \frac{\sigma}{m_v} E^2 \qquad (66)$$

where σ is the material electric conductivity[7]. However, in many situations, these equations are unpractical, even with finite element analysis. The complex nonlinear B(H) characteristic, which is also dependent on the lamination thickness, is the main reason [32]. So, empirical models for core loss evaluation are often considered. The most common is the Steinmetz equation [28]: the following expression for core loss density in a ferromagnetic material (formulated as the sum of hysteresis (P_h) and classic eddy current (P_e) losses) was first achieved:

---

[6] For f [Hz] and m_v [kg/m^3], then P_h [W/kg].

[7] For E [V/m] and σ [S/m], then P_e [W/kg].

$$P_{core} = P_h + P_e = k_h f B_{max}^{1,6} + k_e f^2 B_{max}^2 \tag{67}$$

which is valid in the range of 0.1 T < B_{max} < 1.5 T. Hysteresis and eddy current loss coefficients are, respectively, k_h and k_e, which can be extracted from measured data. They both depend on the core material; k_e also depends on the lamination thickness (d). In fact, k_e has an analytical formulation, which can be derived from Eq. (66):

$$P_e = \frac{\sigma \pi^2 d^2}{6 m_v} f^2 B_{max}^2 \tag{68}$$

An important remark is that Eq. (65) assumes uniform flux density distribution across the lamination thickness. It should be noted that for SRM this is a most relevant limitation. Over the years, Eq. (67) has been upgraded, which brought higher accuracy. Experimental data showed that the measured eddy current losses are higher than P_e. Based on statistical loss theory, Bertotti proposed an additional term to account for the excess losses (P_{ex}), which can be expressed as [33]:

$$P_{ex} = k_{ex} (f \cdot B_{max})^{\frac{3}{2}} \tag{69}$$

where k_{ex} is dependent on the material microstructure, the conductivity, and the cross-sectional area of the lamination. Different theories have been developed to explain excess losses, but this is still under discussion [32].

For the hysteresis term, the power of B_{max} was found later to be dependent on the material type, as well on B_{max}. Therefore, a more accurate expression was adopted for core loss estimation, with a modified hysteresis term (k_h, a, and b are its parameters) and including the excess losses:

$$P_{core} = P_h + P_e + P_{ex} = k_h f B_{max}^{a+b \cdot B_{max}} + k_e (f \cdot B_{max})^2 + k_{ex} (f \cdot B_{max})^{\frac{3}{2}} \tag{70}$$

Further experiments, together with finite element analysis, revealed that it predicts core losses with very good accuracy for $f \le 1500$ Hz and B_{max} < 1 T. For higher flux densities, it gives good results for frequencies up to 400 Hz [32].

4.3.1.3 Core losses under nonsinusoidal and uniform flux densities

Most often, coefficients in Eq. (70) are obtained through curve-fitting techniques, based on manufacturer's core losses. Moreover, the hysteresis term in Eq. (70) is limited to symmetrically flux density variations about zero (i.e., $-B_{max}$ < B < B_{max}) and, most important, without minor loops included in the main hysteresis loop [34]. In short, the previous expression is mostly suited for sinusoidal flux density waveforms, with uniform distributions in the core. For SRM, these conditions are not valid, so different approaches must be considered. Furthermore, parameter for empirical formulas related to nonsinusoidal flux losses must be based on measured core loss values. Manufacturer's data for sinusoidal flux may lead to large errors for nonsinusoidal core loss estimation. In order to consider nonsinusoidal waveforms, the product ($f \cdot B$) is substituted by (dB/dt) in these two terms:

$$P_{core} = k_h f B_{max}^{a+b \cdot B_{max}} + k_e \int_0^T \left(\frac{dB}{dt} \right)^2 dt + k_{ex} \int_0^T \left(\frac{dB}{dt} \right)^{\frac{3}{2}} dt \tag{71}$$

where *T = 1/f*.

However, since SRM usually operates at high frequencies, the influence of skin effect and saturation over eddy current and hysteresis losses cannot be disregarded: it leads to nonuniform field densities, which brings additional challenges for core loss modeling. In order to have accurate estimations, this must be addressed. In the following, a brief discussion about the impact on eddy current and hysteresis losses is addressed.

4.3.1.4 Eddy current losses

The skin effect in the magnetic core is due to the field created by eddy currents: for high frequencies, particularly for thick lamination core, the flux density at the lamination surface is higher than the one at its center; moreover, their waveforms are also displaced [24, 32]. Flux penetration in the lamination is measured by the skin depth penetration (δ): it is the distance from the steel surface, where the field has decreased by a factor of 1/e, and it is approximately given by:

$$\delta = \frac{1}{\sqrt{\pi f \mu \sigma}} \tag{72}$$

where f is the excitation frequency, μ the magnetic permeability, and σ is the material electric conductivity.

Therefore, the magnetic density field has a nonuniform distribution, and it is mainly concentrated on the lamination surface. Eddy current paths have now a higher resistance, meaning that its value and the correspondent losses are smaller, when compared to uniform field densities scenarios. Naturally, this is not foreseen by the previous expressions, which give excessive values. Several models to calculate eddy current loss in electrical machine laminations for nonuniform field density have been proposed [32]. A common approach for a periodic nonsinusoidal flux density waveform is to consider its Fourier series decomposition. The contribution of each harmonic component is calculated based on its frequency and magnitude, through Steinmetz expression. Frequency is particularly relevant, since it determines the skin effect magnitude of the individual harmonics. However, one must not forget that such an approach is based on the superposition principle. In this way, its effectiveness must be always confronted with experimental loss values.

4.3.1.5 Hysteresis losses

Due to SRM geometry and operating conditions (in particular, high frequencies, local saturation, and skin effect), the peak flux density may be very different in several parts of the lamination [24]. This causes local hysteresis loops, i.e., minor loops, in addition to the major loop (**Figure 10**).

As a consequence, several points inside the lamination have different local hysteresis power losses [24, 34], which may lead to core hot spots. It should be noted that a relevant harmonic content in the flux density waveform reflects a significant number of minor loops. Moreover, these additional losses may represent an important proportion of the total hysteresis loss, which stresses the importance of modeling them [35]. A most relevant conclusion in this reference is that minor loop positions inside the main cycle (i.e., the DC flux density value associated to the minor loop) have a significant influence in the hysteresis losses. It should be noted that none of this is considered in the first term of Eq. (71).
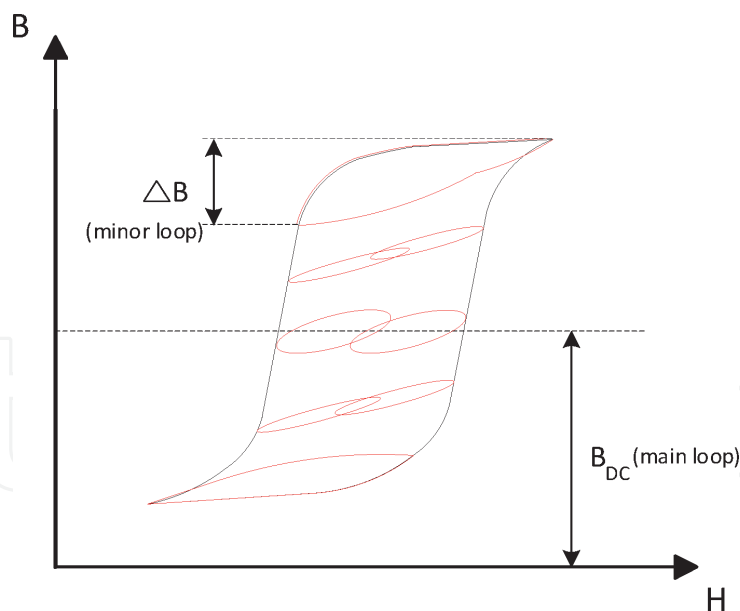
Figure 10.
Hysteresis loops (major in black, minors in red).

Based on experimental studies, minor loop hysteresis loss evaluation has been frequently addressed through empirical formulas [20, 24] (in [20] the Fourier series harmonic decomposition is considered). However, one must be aware that the effectiveness of this approach is attached to certain simplifications and/or to specific flux waveforms. This highlights the fact that for every kind of electrical machine, under specific operation conditions, a particular formula should be addressed. Therefore, a lot of work still need to be done, in order to get accurate methods to estimate hysteresis minor loop losses [24]. These are important issues to be addressed in SRM core loss characterization.

4.3.1.6 Rotational flux losses

Rotational flux densities (due to changes in the flux density vector direction, relatively to a given reference frame) may have important contributions for the total core losses in electrical machines.
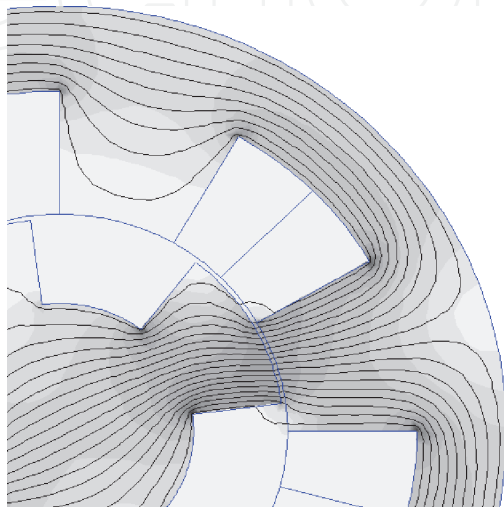

Figure 11.
Magnetic field distribution around stator and rotor tooth.

Particularly in SRM, such rotational flux density variations are well pronounced around the stator and rotor tooth, as represented in **Figure 11**, due to changes on their relative position.

Predicting rotational flux losses is much more complex than alternating flux, with a fixed magnetic axis. Moreover, measuring them is quite complex, since precisely controlled rotational flux density waveforms are difficult to induce in test samples [34].

Some models have been proposed for estimating iron loss under rotational conditions but are based on sinusoidal flux densities. Usually, the flux density vector is decoupled into two orthogonal components, for a given machine region. For each component, losses are independently calculated and then added [36]. Once again, this approach relies on the superposition principle. Due to hysteresis high nonlinearity, it seems reasonable to question the effectiveness of such approach.

5. Conclusions

SRM are simple, rugged, and fault-tolerant machines, with potential to compete with conventional motors. The major drawbacks are torque pulsation and acoustic noise, due to its high nonlinear operation features. In addition, the power converter requires a particular architecture, together with specific control methods. SRM modeling is a challenging task, due to its geometry and operation conditions. Nonetheless, this is a crucial task, since nowadays design and control developments are much dependent on simulation models. Independently of the modeling approach, a key issue is to understand the SRM electromechanical conversion process.

Accurate SRM loss characterization is crucial for designing and control algorithm development. Electrical machines core loss estimation has been supported by empirical models for sinusoidal waveforms. However, this is not suitable for SRM, since flux density waveforms are not sinusoidal and differ from one another, according to the core sections. Moreover, complex magnetic phenomena must be addressed, which are not considered in most empirical models.

This chapter has two main intentions. The first is to present a general view on conventional SRM, where a substantial effort is given on analytical description of electromechanical conversion. The second one is to give an overview on SRM losses—particularly, the iron loss—including the main challenges for characterizing and estimating them.

As a final remark, there are several open challenges in both subjects. A lot of research work still need to be done.

Author details

Pedro Sousa Melo[1]* and Rui E. Araújo[2]

1 School of Engineering, Polytechnic of Porto, Porto, Portugal

2 INESC TEC and Faculty of Engineering, University of Porto, Porto, Portugal

*Address all correspondence to: pma@isep.ipp.pt

IntechOpen

References

[1] Gan C, Wu J, Sun Q, Kong W, Li H, Hu Y. A review on machine topologies and control techniques for low-noise switched reluctance motors in electric vehicle applications. IEEE Access. 2018;**6**:31430-31443

[2] Vrenken R et al. Switched reluctance motor drive for full electric vehicles—Part I: Analysis. In: 2013 8th International Conference and Exhibition on Ecological Vehicles and Renewable Energies (EVER), IEEE. 2013. pp. 1-7

[3] Haghbin S, Rabiei A, Grunditz E. Switched reluctance motor in electric or hybrid vehicle applications: A status review. In: 2013 8th IEEE Conference on Industrial Electronics and Applications (ICIEA); IEEE. 2013. pp. 1017-1022

[4] Rajashekara K. Present status and future trends in electric vehicle propulsion technologies. IEEE Journal of Emerging and Selected Topics in Power Electronics. 2013;**1**(1):3-10

[5] Mamede ACF, Camacho JR, Araújo RE. Influence of geometric dimensions on the performance of switched reluctance machine. Machines. 2019;**7**(4):71

[6] Burkhart B, Klein-Hessling A, Ralev I, Weiss CP, De Doncker RW. Technology, research and applications of switched reluctance drives. CPSS Transactions on Power Electronics and Applications. 2017;**2**(1):12-27

[7] Torkaman H, Moradi R, Hajihosseinlu A, Toulabi M. A comprehensive power loss evaluation for switched reluctance motor in presence of rotor asymmetry rotation: Theory, numerical analysis and experiments. Energy Conversion and Management. 2014;**77**:773-783

[8] Faiz J, Ganji B, Carstensen C, De Doncker R. Loss prediction in switched reluctance motors using finite element method. European Transactions on Electrical Power. 2009;**19**(5):731-748

[9] Miller TJE. Switched Reluctance Motors and their Control. Lebanon, OH: Magna Physics; 1993

[10] Krishnan R. Switched Reluctance Motor Drives: Modeling, Simulation, Analysis, Design, and Applications. CRC Press; 2001. ISBN: 978-084-930-838-3

[11] Miller TJE. Electronic control of switched reluctance machines. newnes. In: Power Engineering Series; 2001. ISBN: 978-075-065-073-1

[12] Ahn J-W. In: Lamchich MT, editor. Switched Reluctance Motor Torque Control. Croatia: IntechOpen; 2011, p. 53. ISBN: 978-953-307-428-3. Available from: http://www.intechopen. com/books/torque-control/switched-reluctance-motor

[13] Hannoun H, Hilairet M, Marchand C. Design of an SRM speed control strategy for a wide range of operating speeds. IEEE Transactions on Industrial Electronics. 2010;**57**(9): 2911-2921

[14] Vujicic VP. Minimization of torque ripple and copper losses in switched reluctance drive. IEEE Transactions on Power Electronics. 2012;**27**(1): 388-399

[15] Ishikawa T, Hashimoto Y, Kurita N. Optimum design of a switched reluctance motor fed by asymmetric bridge converter using experimental design method. IEEE Transactions on Magnetics. 2014;**50**(2):781-784

[16] Ye J, Emadi A. Power electronic converters for 12/8 switched reluctance motor drives: A comparative analysis. In: 2014 IEEE Transportation

Electrification Conference and Expo (ITEC); IEEE. 2014. pp. 1-6

[17] Krause PC, Wasynczuk O, Sudhoff SD, Pekarek S. Analysis of Electric Machinery and Drive Systems. Wiley Online Library; 2002

[18] Torrent M, Andrada P, Blanque B, Martinez E, Perat J, Sanchez J. Method for estimating core losses in switched reluctance motors. European Transactions on Electrical Power. 2011;**21**(1):757-771

[19] Bui MD, Schäfer U. Core losses measurement technique for high frequency and flux density of switched reluctance machines. In: 2012 XXth International Conference on Electrical Machines (ICEM); IEEE. 2012. pp. 1619-1624

[20] Parsapour A, Dehkordi BM, Moallem M. Predicting core losses and efficiency of SRM in continuous current mode of operation using improved analytical technique. Journal of Magnetism and Magnetic Materials. 2015;**378**:118-127

[21] Mokhtari H, Tara E. Efficiency map of a switched reluctance motor using finite element method in vehicular applications. In: 7th International Conference on Power Electronics, 2007. ICPE'07; IEEE. 2007. pp. 644-649

[22] Chindurza I, Dorrell DG, Cossar C. Assessing the core losses in switched reluctance machines. IEEE Transactions on Magnetics. 2005;**41**(10):3907-3909

[23] Rafajdus P, Hrabovcova V, Hudak P. Investigation of losses and efficiency in switched reluctance motor. In: 12th International Power Electronics and Motion Control Conference, 2006 "EPE-PEMC 2006"; IEEE. 2006. pp. 296-301

[24] Ibrahim M, Pillay P. Core loss prediction in electrical machine laminations considering skin effect and minor hysteresis loops. IEEE Transactions on Industry Applications. 2013;**49**(5):2061-2068

[25] Krings A, Nategh S, Stening A, Grop H, Wallmark O, Soulard J. Measurement and modeling of iron losses in electrical machines. In: 5th International Conference Magnetism and Metallurgy WMM'12, June 20th to 22nd, 2012, Ghent, Belgium; Gent University. 2012. pp. 101-119

[26] El-Kharahi E, El-Dessouki M, Lindh P, Pyrhönen J. Toward including the effect of manufacturing processes in the pre-estimated losses of the switched reluctance motor. Ain Shams Engineering Journal. 2015;**6**(1):121-131

[27] Ionel DM, Popescu M, Dellinger SJ, Miller T, Heideman RJ, McGilp MI. On the variation with flux and frequency of the core loss coefficients in electrical machines. IEEE Transactions on Industry Applications. 2006;**42**(3):658-667

[28] Steinmetz C. On the law of hysteresis. Transactions of the American Institute of Electrical Engineers. 1892;**9**(1):1-64

[29] Li J, Abdallah T, Sullivan CR. Improved calculation of core loss with nonsinusoidal waveforms. In: Thirty-Sixth IAS Annual Meeting. Conference Record of the 2001 IEEE; Industry Applications Conference, 2001; IEEE, vol. 4. 2001. pp. 2203-2210

[30] Venkatachalam K, Sullivan CR, Abdallah T, Tacca H. Accurate prediction of ferrite core loss with nonsinusoidal waveforms using only Steinmetz parameters. In: IEEE Workshop on Computers in Power Electronics, vol. 2002. 2002. pp. 36-41

[31] Aguglia D, Neuhaus M. Laminated magnetic materials losses analysis under non-sinusoidal flux waveforms in power

electronics systems. In: 2013 15th European Conference on Power Electronics and Applications (EPE); IEEE. 2013. pp. 1-8

[32] Zhang Y, Pillay P, Ibrahim M, Cheng M-C. Magnetic characteristics and core losses in machine laminations: High-frequency loss prediction from low-frequency measurements. IEEE Transactions on Industry Applications. 2012;**48**(2):623-629

[33] Bertotti G. Hysteresis in Magnetism: For Physicists, Materials Scientists, and Engineers. Academic Press; 1998. ISBN: 978-012-093-270-2

[34] Calverley SD, Jewell GW, Saunders RJ. Prediction and measurement of core losses in a high-speed switched-reluctance machine. IEEE Transactions on Magnetics. 2005; **41**(11):4288-4298

[35] Simão C, Sadowski N, Batistela N, Kuo-Peng P. Simplified models for magnetic hysteresis losses evaluation in electromagnetic devices. In: Electric Machines and Drives Conference, 2009. IEMDC'09. IEEE International; IEEE. 2009. pp. 876-880

[36] Hernandez-Aramburo CA, Green TC, Smith AC. Estimating rotational iron losses in an induction machine. IEEE Transactions on Magnetics. 2003;**39**(6):3527-3533